

Galactic Isolated Stellar-Mass Black Holes with the Magnetospheric Spark Gap as Possible GeV-TeV Gamma-ray Unidentified Sources

KOKI KIN ¹, RIKU KUZE ¹, AND SHIGEO S. KIMURA ^{1,2}

¹*Astronomical Institute, Graduate School of Science, Tohoku University, Sendai 980-8578, Japan*

²*Frontier Research Institute for Interdisciplinary Sciences, Tohoku University, Sendai 980-8578, Japan*

ABSTRACT

Billions of isolated stellar-mass black holes (IBHs) are thought to wander through the interstellar medium (ISM) in the Galaxy, yet only one has been detected. IBHs embedded in ISM would accrete gas via Bondi-Hoyle-Littleton accretion, and with efficient magnetic flux accumulation, the magnetosphere would be formed in the vicinity of IBHs. We explore the detectability of such IBHs through high-energy gamma rays from spark gaps in their magnetospheres based on our recent numerical simulation. The gap gamma rays can be bright at the GeV-TeV energies when IBHs are in the dense ISM. About 10^3 and 10 IBHs might be contained in unidentified objects of the *Fermi* Large Area Telescope and the High Energy Stereoscopic System, respectively. A future Galactic plane survey by the Cherenkov Telescope Array Observatory would lead to $\sim 10^2$ detections. We also evaluate the combined gamma-ray emission of IBHs in the Galaxy and find that the IBHs may contribute to the Galactic diffuse gamma rays. IBHs will emit optical and X-ray photons from their accretion disk as counterparts, potentially useful for identifying candidates.

Keywords: Black Holes (162) — Accretion (14) — Gamma-Ray Sources (633) — Plasma Astrophysics (1261)

1. INTRODUCTION

The existence of stellar-mass black holes (BHs) has been confirmed through decades of observations of Galactic X-ray binaries (see Corral-Santana et al. 2016; Tetarenko et al. 2016), increasing numbers of gravitational wave detections from compact binary mergers (Abbott et al. 2023), and the analysis of the dynamical motion of binaries in *Gaia* data (Gaia BH 1, 2, and 3; El-Badry et al. 2023a,b; Gaia Collaboration et al. 2024). 10^8 - 10^9 stellar-mass BHs are thought to exist in the Galaxy as the end products of massive ($\gtrsim 25M_\odot$) stars (e.g. Shapiro & Teukolsky 1986; Caputo et al. 2017), and the governing fraction of them are expected to be isolated stellar-mass BHs (IBHs) (Olejak et al. 2020). However, we have not detected any hints of electromagnetic signatures related to IBHs, except for one microlensing event (OGLE-2011-BLG-0462/MOA-2011-BLG-191; Sahu et al. 2022; Lam et al. 2022).

IBHs around the Galactic plane would accrete interstellar medium (ISM) via the Bondi-Hoyle-Littleton (BHL) accretion (see Edgar 2004, for a review). The non-zero net angular momentum of infalling gas will force them to form the accretion disks around IBHs

(Shapiro & Lightman 1976; Fujita et al. 1998; Agol & Kamionkowski 2002; Ioka et al. 2017). In a typical ISM environment, the BHL accretion rate onto IBHs is so low that their accretion disk would be a radiatively inefficient accretion flow (RIAF; Ichimaru 1977; Narayan & Yi 1994; Yuan & Narayan 2014). The accreting gas in RIAF is hot, which leads them to achieve a high radial velocity. As a result, an efficient accumulation of the magnetic flux onto IBHs is expected (Cao 2011; Barkov et al. 2012; Ioka et al. 2017). The disk near the IBH will thus be the magnetically arrested disk (MAD; Narayan et al. 2003, 2012), in which the magnetic flux threading the central BH is at a saturated level. Recent general relativistic magnetohydrodynamic (GRMHD) simulations (Kaaz et al. 2023; Kwan et al. 2023; Galishnikova et al. 2024; Kim & Most 2024) support this scenario. The detectability of the IBHs via multi-wavelength emission from accretion disks, disk-induced outflows, and jets has been investigated in many literatures (e.g., Barkov et al. 2012; Fender et al. 2013; Tsuna et al. 2018; Tsuna & Kawanaka 2019; Kimura et al. 2021a).

At the inner edge of the MAD, accretion is truncated by the magnetic pressure, and the magnetosphere is formed. We have recently investigated the plasma dy-

namics in the magnetosphere of the stellar-mass BHs using one-dimensional general relativistic particle-in-cell (GRPIC) simulations (Kin et al. 2024). We have shown that the longitudinal electric field (i.e. the spark gap) emerges during the charge-starved state of the magnetosphere, as is the case for several previous research (see, e.g., Levinson & Cerutti 2018; Kisaka et al. 2020; Crinquand et al. 2020; Chen & Yuan 2020; Kisaka et al. 2022; Hirotani et al. 2022). The spark gap efficiently accelerates the electrons, emitting high-energy gamma rays. We have also studied the range of the mass accretion rate that brightens gamma-ray emission. Our analysis has suggested that gamma rays escaping from IBH magnetospheres embedded in the dense ISM are bright enough for detection by the *Fermi* Large Area Telescope (LAT; Atwood et al. 2009), the High Energy Stereoscopic System (H.E.S.S.; Aharonian et al. 2006), and the Cherenkov Telescope Array Observatory (CTAO; Cherenkov Telescope Array Consortium et al. 2019)).

In this work, we further explore this scenario and thoroughly discuss the detection prospects of signals from MADs/spark gaps of IBHs. The paper is organized as follows: Section 2 gives a method for our calculations. Then, we show the results of the expected number, physical properties, and spectral properties of detectable IBHs in Section 3. Section 4 discusses the identification strategy and caveats. Finally, conclusions are given in Section 5. We have also performed the 1D GRPIC simulations with various BH spin values to investigate the dependence of gamma-ray luminosity on the spin. Simulation results are summarized in Appendix B. Here and hereafter we use the convention $Q_x = (Q/10^x)$ in cgs units, except for the BH mass, $M = 10^x M_x M_\odot$.

2. METHOD

2.1. Model Overview

We consider Galactic IBHs wandering through the ISM. Fig. 1 provides the schematic image of our model. IBHs accrete ISM and the accretion disk is formed. The disk near IBHs will be the MAD due to efficient magnetic flux accumulation, and then the magnetosphere is formed around the IBHs.

The BHL mass accretion rate for each IBH is estimated as a function of the BH mass, M , the BH proper motion velocity, v , and the ISM number density, n_{ISM} ,

$$\begin{aligned} \dot{M}(M, v, n_{\text{ISM}}) &= \lambda_w \frac{4\pi G^2 M^2 \mu m_p n_{\text{ISM}}}{V_{\text{rela}}^3} \\ &\simeq 1.7 \times 10^{14} \lambda_{w,0} M_1^2 \left(\frac{\mu}{1.26} \right) n_{\text{ISM},1} V_{\text{rela},6.3}^{-3} \text{g s}^{-1}, \end{aligned} \quad (1)$$

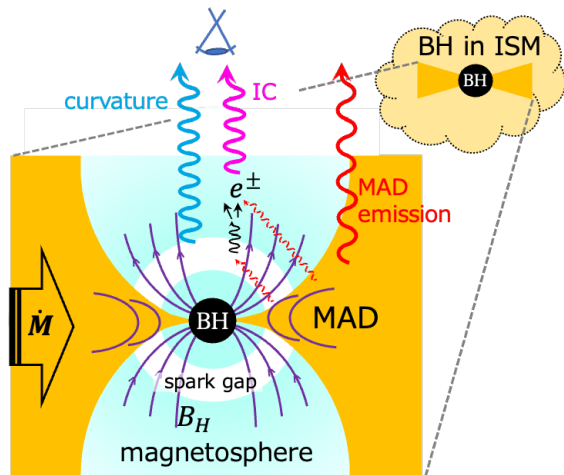


Figure 1. Schematic image of the IBH-MAD-magnetosphere system.

where m_p is the proton mass, μ is the mean molecular weight, G is the gravitational constant, λ_w is the wind mass loss rate, and $V_{\text{rela}} = (c_{s,\text{ISM}}^2 + v^2)^{1/2}$ is the IBH relative velocity considering the effective sound velocity of ISM, $c_{s,\text{ISM}}$. We focus on \dot{M} in the sub-Eddington regime, in which we expect a MAD formation: $\dot{m} \equiv \dot{M}/\dot{M}_{\text{Edd}} \leq 10^{-2}$, where $\dot{M}_{\text{Edd}} = 4\pi G M m_p / \sigma_T c \simeq 1.4 \times 10^{18} M_1 \text{g s}^{-1}$ is the Eddington mass accretion rate. (σ_T is the Thomson cross section and c is the speed of light.) This condition is satisfied for most of the parameter ranges in this work. (compare Eq. (1) with \dot{M}_{Edd} .) We then consider emissions from two regions: the MADs and the spark gaps in the magnetospheres. MAD multi-wavelength emission properties are sensitive to \dot{M} . Gap gamma-ray emission properties are also determined by \dot{M} , and additionally, by the BH spin, a (see Section 2.6).

In the actual calculation, we first determine the spatial and the velocity distribution of IBHs in the Galaxy through the simplified dynamical calculation (Section 2.2). Each IBH's spatial correlation probability between ISM i.e. the volume filling factor, ξ , can be derived as a function of n_{ISM} and IBH's position in the Galaxy, considering the ISM's spatial distribution. Then, we give each IBH a mass and a spin (Section 2.3). The IBH-MAD/spark gap multi-wavelength emission spectra for a given n_{ISM} are calculated by using those parameters (Sections 2.4, 2.5, and 2.6). The observed flux of each IBH is calculated based on its position in the Galaxy. We discuss the possible reduction of the persistent gamma-ray flux due to the expected time-dependency of the spark gap in Section 2.7.

2.2. IBH Distribution Calculation

We calculate the distribution of BHs in 2D cylindrical coordinates perpendicular to the Galactic plane,

Table 1. Physical parameters of ISM. n_{ISM} is the reference value of the ISM number density, $c_{s,\text{ISM}}$ is the effective sound velocity, h_{ISM} is the pressure scale height, $\xi(R_{\text{obs}})$ is the calculated volume filling factor at the Sun’s location, and $\dot{m}(M_1, v_6)$ is the Eddington ratio calculated using $M = 10M_{\odot}$, $v = 10 \text{ km s}^{-1}$, and reference values of n_{ISM} and $c_{s,\text{ISM}}$.

ISM Phase	$n_{\text{ISM}} [\text{cm}^{-3}]$	$c_{s,\text{ISM}} [\text{km s}^{-1}]$	$h_{\text{ISM}} [\text{kpc}]$	$\xi(R_{\text{obs}})$	$\dot{m}(M_1, v_6)$
Molecular Clouds	$10^2, 10^3$	$3.7(n_{\text{ISM}}/100 \text{ cm}^{-3})^{-0.35}$	0.075	$3.9 \times 10^{-3}, 6.2 \times 10^{-5}$	$3.2 \times 10^{-2}, 2.8 \times 10^{-3}$
Cold HI	10	10	0.15	0.061	1.2×10^{-4}
Warm HI	0.3	10	0.5	0.37	3.6×10^{-6}

(R, z) , following the method described in Tsuna et al. (2018). To reduce the computational time, we calculate 10^5 IBHs and scale the result to the estimated IBH total number in the Galaxy, $N_{\text{tot}} = 10^8$ (see Section 3.1). One important parameter for the calculation is the IBH initial velocity, mostly determined by the kick from the supernova explosion. We assume the kick velocity distribution as the 3D Maxwell-Boltzmann distribution with a mean kick velocity v_{avg} . We run the calculation for $v_{\text{avg}} = \{10, 50, 100, 400\} \text{ km s}^{-1}$, which are consistent with the range of the kick velocity estimated from the BH X-ray binary distribution in the Galaxy (e.g. Repetto et al. 2017; Nagarajan & El-Badry 2024). We note that we have introduced the smoothing terms in the equations of motion to reduce numerical errors on the calculated BH velocity. More details for the calculation and the resultant spatial/velocity distributions for different values of v_{avg} are shown in Appendix A. Overall results are consistent with Tsuna et al. (2018): the IBH spatial distribution approaches from the initial exponential disk shape to a more spherical shape for $v_{\text{avg}} \geq 100 \text{ km s}^{-1}$. In contrast, the exponential disk profile is preserved for lower v_{avg} cases.

2.3. ISM Property, Distance, Mass, & Spin

We consider three ISM phases of different temperatures and the density (Bland-Hawthorn & Reynolds 2000), which are molecular clouds, cold neutral medium (cold HI), and warm neutral medium (warm HI).¹ Parameters are enlisted in Table 1. The ISM volume filling factor for a number density of the certain ISM phase at a given position is described as $\xi(n_{\text{ISM}}; R, z) = \int d\xi/dn_{\text{ISM}}(n_{\text{ISM}}; R)H(h_{\text{ISM}} - z)dn_{\text{ISM}}$, where H denotes the Heaviside function. The differential fraction $d\xi/dn_{\text{ISM}}$ is obtained by considering the n_{ISM} dependence of ξ for molecular and cold HI gas, and the observed cylindrical distribution of the ISM column den-

sity in the Galactic disk (see Agol & Kamionkowski 2002; Tsuna et al. 2018, for details).

We must then set the distance, mass, and spin for each IBH to calculate the radiation flux. The angle between the observer and each IBH concerning the center in the Galactic plane, θ_{BH} , is given uniformly. Then, the distance between observer and IBHs is $d = [(R^2 + R_{\text{obs}}^2 - 2RR_{\text{obs}} \cos \theta_{\text{BH}}) + z^2]^{1/2}$, where $R_{\text{obs}} = 8.3 \text{ kpc}$ is the observer distance from the Galactic center. The IBH mass function is set as a power-law shape, $dN/dM \propto M^{-\alpha_m}$ ($\alpha_m \approx 3.5$), which mimics the primary mass distribution obtained from the gravitational wave observation of binary-BH (BBH) mergers (Abbott et al. 2023). Minimum and maximum IBH masses are chosen from their posterior values of parameters in the fitting function, $M_{\text{min}} \sim 5.0M_{\odot}$, $M_{\text{max}} \sim 87M_{\odot}$. As for the IBH spin, we use two distinct models of the spin populations based on current observational constraints. One is the *low spin* model, which is set to reproduce the BBH primary spin probability distribution $P_{\beta}(a) \propto a^{\alpha_a - 1}(1 - a)^{\beta_a - 1}$ ($\alpha_a = 2.0$, $\beta_a = 5.0$; Abbott et al. 2023), and peaks around $a \sim 0.2$. The other is the *high spin* model, reproducing the spin distribution obtained from the spectral analysis of Galactic BH X-ray binaries. We fit the spin data of 36 NuSTAR-detected BH X-ray binaries in Draghis et al. (2024) with a function $P_{\text{LN}}(a) \propto \exp[-(\log(1.0 - a) - \mu_a)^2 / (2\sigma_a^2)] / [(1.0 - a)\sqrt{2\pi\sigma_a^2}]$ and obtain $\{\mu_a, \sigma_a\} = \{-2.67, 0.70\}$. To maintain accountability with the number of IBH samples (10^5) much lower than $N_{\text{tot}} = 10^8$, we repeat the random sampling of θ_{BH} , M , and a one-hundred times with a different seed for each BH, and combine all realizations to obtain the final result.

2.4. Radiation Flux from IBH-MADs

The next step is to calculate radiation flux from IBH-MADs. We calculate radiation spectra by the method described in Kimura & Toma (2020); Kimura et al. (2021a,b); Kuze et al. (2022, 2024). We assume that the magnetic reconnection in the MADs heats plasma and produces non-thermal particles. We consider synchrotron emission and Comptonization via thermal elec-

¹ We have checked that IBHs in warm HII and hot HII could not achieve high \dot{M} enough to contribute to the detection.

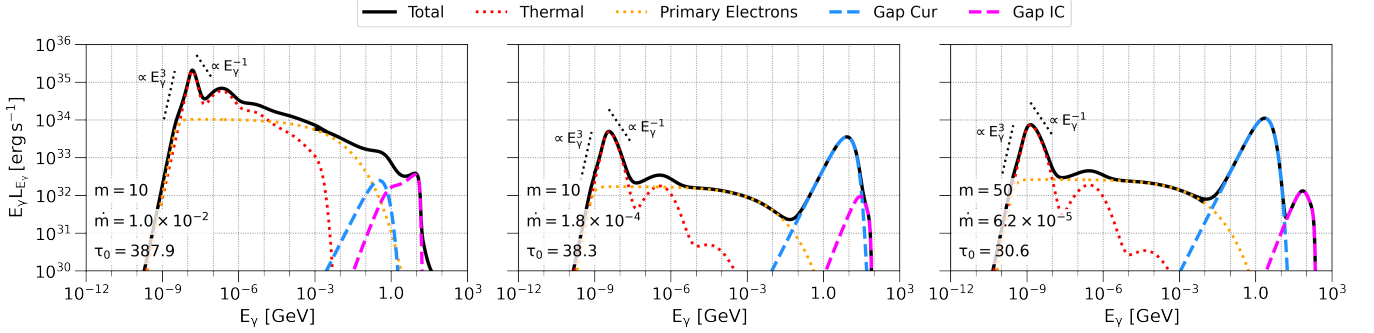


Figure 2. The multi-wavelength luminosity spectra of the IBH-MAD/spark gap for $a = 0.9$. Each panel shows the results for $(m = M/M_\odot, \dot{m}) = (10, 1.0 \times 10^{-2}), (10, 1.8 \times 10^{-4}), (50, 6.2 \times 10^{-5})$. The black solid line denotes the total spectrum. The dotted lines show synchrotron emission from MAD thermal electrons (red) and non-thermal primary electrons (orange). The dashed lines show spark gap curvature radiation (cyan) and IC up-scattering emission components (magenta).

trons, synchrotron emissions from primary electrons and protons, and synchrotron emissions from secondary-produced electrons/positrons via the Bethe-Heitler process and the two-photon annihilation.

The size of MAD is set as $R_{\text{MAD}} = \mathcal{R}_{\text{MAD}} r_g$ ($\mathcal{R}_{\text{MAD}} = 10$), where $r_g = GM/c^2$ is the BH gravitational radius. The magnetic field and the proton number density in the MAD, B and N_p , respectively, are derived as functions of M and \dot{M} for the fixed viscosity parameter $\alpha \approx 0.3$ (cf. Shakura & Sunyaev 1973) and plasma beta $\beta = 0.1$. The fraction of the dissipated energy to the accretion flow gravitational energy is $\epsilon_{\text{dis}} = 0.15$, and that of the non-thermal particle energy to the dissipated energy is $\epsilon_{\text{NT}} = 0.33$. The thermal electrons heating ratio compared to protons is calculated by using the prescription from Rowan et al. (2017); Chael et al. (2018), $f_e \approx 0.5 \exp[-(1 - 4\beta\sigma_B)/(0.8 + \sqrt{\sigma_B})]$, where $\sigma_B = B^2/4\pi N_p m_p c^2 \simeq 0.5 \mathcal{R}_{\text{MAD},1}^{-1} \beta_{-1}^{-1}$ is the magnetization parameter. Then, the electron heating rate can be estimated as

$$Q_{e,\text{thermal}} = f_e \epsilon_{\text{dis}} (1 - \epsilon_{\text{NT}}) \dot{M} c^2 \simeq 3.7 \times 10^{33} \left(\frac{f_e \epsilon_{\text{dis}} (1 - \epsilon_{\text{NT}})}{0.3 \cdot 0.15 \cdot 0.67} \right) \dot{m}_{-4} M_1 \text{ erg s}^{-1}. \quad (2)$$

The electron temperature normalized by the electron rest mass, $\theta_e = kT_e/m_e c^2$ (k is the Boltzmann constant), can be approximated by equating $Q_{e,\text{thermal}}$ and the cooling rate via synchrotron radiation, $E_\gamma L_{E_\gamma}$.² The MADs are mostly optically thick for synchrotron self-absorption by thermal electrons for our current set of parameters. Then, we can estimate $E_\gamma L_{E_\gamma}$ by using the

² We consider cooling by thermal Comptonization as well, but is sub-dominant for current set of parameters.

expression for the Rayleigh-Jeans low-energy tail as

$$E_\gamma L_{E_\gamma} \approx E_{\gamma,\text{syn,pk}} L_{E_{\gamma,\text{syn,pk}}} \sim E_{\gamma,\text{syn,pk}} \cdot 4\pi^2 R_{\text{MAD}}^2 \cdot \frac{2m_e E_{\gamma,\text{syn,pk}}^2}{h^3} \theta_e, \quad (3)$$

where $E_{\gamma,\text{syn,pk}} = x_M (3heB\theta_e^2/4\pi m_e c)$ is the peak energy, x_M is the factor representing the deviation of the actual spectral peak from the synchrotron characteristic frequency (see Mahadevan 1997), h is the Planck constant, and e is the electric charge. Therefore, from Eqs. (2) and (3), we obtain $\theta_e \simeq 1.5 \dot{m}_{-4}^{-1/14} M_1^{1/14} \mathcal{R}_{\text{MAD},1}^{1/4} \alpha_{-0.5}^{3/14} \beta_{-1}^{3/14} x_{M,2}^{-3/7}$, and the corresponding peak energy is

$$E_{\gamma,\text{syn,pk}} \simeq 2.2 \dot{m}_{-4}^{5/14} M_1^{-5/14} \mathcal{R}_{\text{MAD},1}^{-3/4} \times \alpha_{-0.5}^{-1/14} \beta_{-1}^{-1/14} x_{M,2}^{1/7} \text{ eV}. \quad (4)$$

We also introduce $\tau_0 = n_0 \sigma_T r_g$ (n_0 denotes the peak photon number density), which characterizes the radiative compactness for the size of the region in the magnetosphere where MAD thermal photons are dense, $r \lesssim R_{\text{MAD}}$ (see Section 2.5). Due to the narrow spectral shape of thermal synchrotron photons ($E_\gamma L_{E_\gamma} \propto E_\gamma^3$ for $E_\gamma < E_{\gamma,\text{syn,pk}}$ and decaying exponentially comparable to/faster than $\propto E_\gamma^{-1}$ above there, see Fig. 2), we can evaluate it as

$$\tau_0 = \frac{4\pi}{c} \frac{E_{\gamma,\text{syn,pk}} L_{E_{\gamma,\text{syn,pk}}}}{4\pi^2 R_{\text{MAD}}^2 E_{\gamma,\text{syn,pk}}} \sigma_T r_g \simeq 50 \dot{m}_{-4}^{9/14} M_1^{5/14} \mathcal{R}_{\text{MAD},1}^{-5/4} \alpha_{-0.5}^{1/14} \beta_{-1}^{1/14} x_{M,2}^{-1/7}. \quad (5)$$

The number distributions of non-thermal particle species i are derived from the energy transport equation with one-zone steady-state approximations, including injection, cooling, and escaping processes (Eq.(3) of Kimura & Toma 2020). The injection term is given by $\dot{N}_{E_i,\text{inj}} \propto E_i^{-s_{\text{inj}}} \exp(-E_i/E_{i,\text{cut}})$, where $E_{i,\text{cut}}$ is the

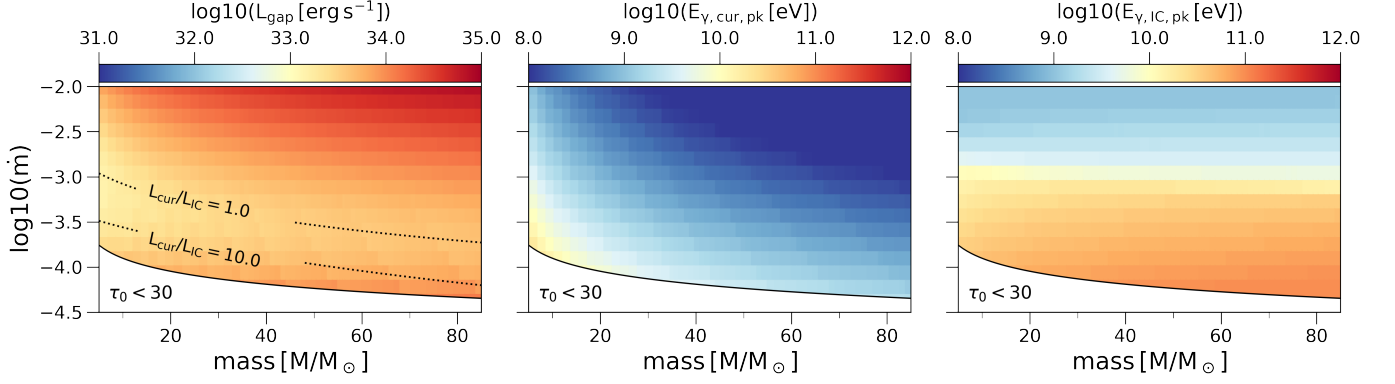


Figure 3. Color maps for L_{gap} (left), $E_{\gamma,\text{cur,pk}}$ (middle), and $E_{\gamma,\text{IC,pk}}$ (right) as functions of M and m , with $a = 0.9$.

cutoff energy. We use $s_{\text{inj}} = 2$ based on the long-term 3D PIC simulation (Zhang et al. 2023), which is different from that used in Kimura et al. (2021a). The luminosities of non-thermal components are determined to satisfy $\int \dot{N}_{E_p,\text{inj}} E_p dE_p \approx \epsilon_{\text{dis}} \epsilon_{\text{NT}} \dot{M} c^2$ for protons and $\int \dot{N}_{E_e,\text{inj}} E_e dE_e \approx f_e \epsilon_{\text{dis}} \epsilon_{\text{NT}} \dot{M} c^2$ for electrons, respectively.

In Fig. 2, we demonstrate the IBH-MAD spectra for $(M/M_\odot, \dot{m}) = (10, 1.0 \times 10^{-2})$, $(10, 1.8 \times 10^{-4})$, $(50, 6.2 \times 10^{-5})$. Thermal synchrotron emission produces the peak around the optical-UV band (Eq. (4)). Several humps in around $10\text{-}10^3$ eV are produced by thermal Comptonization. The primary electrons' non-thermal synchrotron emission dominates the spectrum from keV to MeV. Synchrotron emission from primary protons and secondary-produced electrons/positrons peak around the MeV-GeV band but are sub-dominant for most of the parameter range of our interest. (Thus not depicted in the figure.)

2.5. Spark Gap Dynamics & Relation to MAD Properties

Here, we evaluate the physical quantities of the magnetosphere and highlight its relation to the MAD. The magnetic field at the horizon, B_{H} , is set by the magnetic flux accumulation rate, which depends on \dot{M} . Based on the results from GRMHD simulations (e.g. Tchekhovskoy et al. 2011; Narayan et al. 2012), we can evaluate it as $B_{\text{H}} = \phi \sqrt{\dot{M} c} / 2\pi r_{\text{g}} \simeq 1.1 \times 10^7 (\phi/50) \dot{m}_{-4}^{1/2} M_1^{-1/2}$ G, where ϕ is the saturated fraction of the normalized magnetic flux. Inside the magnetosphere, the extraction of the BH rotation energy as the Poynting flux, i.e. the Blandford-Znajek (BZ) process (Blandford & Znajek 1977) is onset. The total Poynting

luminosity via the BZ process, L_{BZ} , is evaluated as

$$L_{\text{BZ}} = \frac{\kappa_{\text{B}} \pi c}{4} a^2 B_{\text{H}}^2 r_{\text{g}}^2 \simeq 2.7 \times 10^{35} \left(\frac{\kappa_{\text{B}}}{0.053} \right) \left(\frac{\phi}{50} \right)^2 \left(\frac{a}{0.9} \right)^2 \dot{m}_{-4} M_1 \text{ erg s}^{-1}, \quad (6)$$

where $\kappa_{\text{B}} = 0.053$ is the empirical factor for the split-monopole field configuration (Tchekhovskoy et al. 2010). A fraction of this energy input to the magnetosphere will be converted to radiation in the spark gap.

The electron-positron pair production will modify the charge/current distribution in the magnetosphere, thereby controlling the spark gap dynamics and the peak amplitude of the gap electric field. The pair production by two MeV energy photons emitted from MADs is sub-dominant (see Levinson & Rieger 2011; Hirotani & Pu 2016; Hirotani et al. 2018; Kin et al. 2024, but also Wong et al. 2021). Thus, we mainly consider the reaction between high-energy gamma rays emitted by gap-accelerated particles and MAD thermal synchrotron photons. The pair production optical depth for a gamma-ray photon of the energy $E_{\gamma,\text{g}}$ in $r \leq R_{\text{MAD}}$ can be evaluated by using the thermal synchrotron photon number density, $n_{\gamma,\text{syn}}(E_{\gamma,\text{syn}})$, and the cross-section, $\sigma_{\gamma\gamma}(E_{\gamma,\text{syn}}, E_{\gamma,\text{g}})$, as

$$\tau_{\gamma\gamma,\text{MAD}}(E_{\gamma,\text{g}}) = n_{\text{syn}}(E_{\gamma,\text{syn}}) \sigma_{\gamma\gamma}(E_{\gamma,\text{syn}}, E_{\gamma,\text{g}}) R_{\text{MAD}} \approx 0.1 \mathcal{R}_{\text{MAD}} \tau_0 \cdot \tilde{n}_{\text{syn}}(x) \cdot \left(\frac{E_{\gamma,\text{syn}} E_{\gamma,\text{g}}}{m_e^2 c^4} \right)^{-1}. \quad (7)$$

In the second line, n_{syn} is normalized as $n_{\text{syn}}(E_{\gamma,\text{syn}}) = n_0 \tilde{n}_{\text{syn}}(x)$ ($x \equiv E_{\gamma,\text{syn}}/E_{\gamma,\text{syn,pk}}$), and $\sigma_{\gamma\gamma}$ is substituted by the asymptotic expression, $\sigma_{\gamma\gamma}(E_{\gamma,\text{syn}}, E_{\gamma,\text{g}}) \approx 0.1 \sigma_{\text{T}} [E_{\gamma,\text{syn}} E_{\gamma,\text{g}} / (m_e^2 c^4)]^{-1}$ (for $E_{\gamma,\text{syn}} E_{\gamma,\text{g}} \gtrsim m_e^2 c^4$). $E_{\gamma,\text{syn}}$ is determined to maximize $\tau_{\gamma\gamma,\text{MAD}}$, and thus should satisfy the condition $E_{\gamma,\text{syn}} = \max\{E_{\gamma,\text{syn,pk}}, E_{\gamma,\text{g}}^{-1} m_e^2 c^4\}$. By substituting τ_0 obtained from Eq. (5), we can expect $\tau_{\gamma\gamma,\text{MAD}} \gtrsim 1$ for interaction

with $E_{\gamma,\text{syn}} \sim E_{\gamma,\text{syn,pk}}$ soft photons and gamma-ray photons with the energy $E_{\gamma,\text{g}} \sim E_{\gamma,\text{syn,pk}}^{-1} m_e^2 c^4 \simeq 117$ GeV when $M \gtrsim 10M_\odot$ and $\dot{m} \gtrsim 10^{-4}$, meaning that gamma-ray photons of this energy could produce electron-positron pairs in the magnetosphere. This is consistent with our GRPIC simulation (Kin et al. 2024), in which the spark gap exhibits a steady quasi-periodic oscillation for $\tau_0 \geq 30$ and bright gamma rays via the curvature process and inverse Compton (IC) up-scattering of MAD optical photons were emitted. We developed empirical relations between τ_0 and averaged values of various physical quantities during the oscillating state, including maximum electron energy, $\gamma_{e,\text{max}}$, and radiation efficiencies for curvature and IC radiation, $L_{\text{cur,pk}}/L_{\text{BZ}}$ and $L_{\text{IC,pk}}/L_{\text{BZ}}$, respectively: $\gamma_{e,\text{max}} \approx 8.9 \times 10^6 (\tau_0/30)^{-2/5}$, $L_{\text{cur,pk}} \approx 10^{-2} (\tau_0/30)^{-14/5} L_{\text{BZ}}$, and $L_{\text{IC,pk}} \approx 5.8 \times 10^{-4} L_{\text{BZ}} \propto \tau_0^{-1/5}$. Those relations are weakly dependent on the shape of the soft photon spectrum and a (see Kin et al. 2024, and also Appendix B of this paper), especially for $\tau_0 \lesssim 100$, for which bright gamma-ray emission is expected. Therefore, we hereby use those empirical relations for all ranges of parameters to derive the persistent gamma-ray flux.

2.6. Radiation Flux from IBH Spark Gaps

Using L_{BZ} , τ_0 , and the empirical relation from our simulation, we calculate the gamma-ray emission spectra from the IBH spark gaps, partially following the method described in Appendix B of Kin et al. (2024). The characteristic energy of curvature emission from $\gamma_e \sim \gamma_{e,\text{max}}$ particles in the gap is calculated as

$$E_{\gamma,\text{cur,pk}} = \frac{3}{4\pi} \frac{hc}{r_g} \gamma_{e,\text{max}}^3 \simeq 7.7 \left(\frac{\tau_0}{50}\right)^{-6/5} M_1^{-1} \text{ GeV}, \quad (8)$$

where the characteristic curvature radius of the magnetic field is assumed to be r_g . You can see that $E_{\gamma,\text{cur,pk}}^{-1} m_e^2 c^4 > E_{\gamma,\text{syn,pk}}$. By substituting a rough approximation $\tilde{n}_{\text{syn}}(x) \sim x^{-2}$ (for $x \geq 1$, see Fig. 2) into Eq. (7), we obtain $\tau_{\gamma\gamma,\text{MAD}}(E_{\gamma,\text{cur,pk}}) \simeq 0.2 (\tau_0/50)^{-7/5} (E_{\gamma,\text{syn,pk}}/2.2 \text{ eV})^2 M_1^{-2} \mathcal{R}_{\text{MAD},1}$. Combining with a negative \dot{m} dependence of $E_{\gamma,\text{cur,pk}}$ (see Eqs. (4) and (5)), we can expect that the most of curvature photons escape from the system. On the other hand, the energy of photons up-scattered by $\gamma_e \sim \gamma_{e,\text{max}}$ particles is $\gamma_{e,\text{max}} m_e c^2 \simeq 3.7 (\tau_0/50)^{-2/5}$ TeV (assuming the reaction in the Klein-Nishina regime), and then $\tau_{\gamma\gamma,\text{MAD}}(\gamma_{e,\text{max}} m_e c^2) \sim 1.6 (\tau_0/50)^{7/5} (E_{\gamma,\text{syn,pk}}/2.2 \text{ eV})^{-1} \mathcal{R}_{\text{MAD},1} > 1$. Secondary-produced pairs will repeat a similar interaction sequence until $\tau_{\gamma\gamma,\text{MAD}}$ becomes $\lesssim 1$. The cutoff energy of IC emission spectra, $E_{\gamma,\text{IC,pk}}$, is determined

as

$$E_{\gamma,\text{IC,pk}} \simeq 17 \left(\frac{\tau_0}{50}\right)^{-1/2} \left(\frac{E_{\gamma,\text{syn,pk}}}{2.2 \text{ eV}}\right)^{-1} \mathcal{R}_{\text{MAD},1} \text{ GeV}, \quad (9)$$

where we assumed that $E_{\gamma,\text{syn}} \sim E_{\gamma,\text{IC,pk}}^{-1} m_e^2 c^4$. In the actual calculation, we use the expression of $\sigma_{\gamma\gamma}$ in Coppi & Blandford (1990) to obtain $E_{\gamma,\text{IC,pk}}$.

Fig. 3 shows the dependence of $L_{\text{gap}} = L_{\text{cur,pk}} + L_{\text{IC,pk}}$, $E_{\gamma,\text{cur,pk}}$, and $E_{\gamma,\text{IC,pk}}$ on M and \dot{m} for $a = 0.9$. L_{gap} for $\dot{m} \gtrsim 10^{-4}$ is around $10^{33} - 10^{35} \text{ erg s}^{-1}$. Both components peak in 1-100 GeV for $\dot{m} \sim 10^{-3} - 10^{-4}$, meaning GeV-TeV detectable IBHs are in this \dot{m} regime. The white-filled region shows $\tau_0 < 30$. The gap gamma-ray spectra for $a = 0.9$ are demonstrated with cyan and magenta dashed lines in Fig. 2. Gap gamma-ray emissions are typically brighter than MAD emission components in GeV-TeV for our current parameter sets. Thus, we focus on the detectability of gap emission in the GeV-TeV band.

2.7. Observed Flux Calculation

After the consideration above, the intrinsic radiation flux for each IBH is obtained as the function of M , v , n_{ISM} , a , and d , assuming that emissions from both MADs and magnetospheric gaps are isotropic (but see Section 4.3). Now, we discuss the attenuation and reduction of gamma-ray fluxes. Gap gamma-ray photons could interact with protons in the ambient gas via the Bethe-Heitler process, but will be negligible for gas clouds with the column density of $N_{\text{H}} \lesssim 10^{22} \text{ cm}^{-2}$ due to its low cross section, $\sigma_{\text{BH}} \sim 10^{-26} \text{ cm}^2$. Attenuation by photons emitted from ambient gas, interstellar radiation field, extragalactic background light, and cosmic microwave background radiation will also be present. Still, it will only be effective at $\gtrsim 100$ TeV (e.g. Veronetti & Lipari 2016). Therefore, we only consider the reduction in the observed gamma-ray flux due to the intermittency of the gap: the gap opens with a typical duration $t_{\text{gap}} \sim 1-10 r_g/c \sim 10^{-4}-10^{-3} M_1 \text{ s}$ during the oscillating state (see Chen & Yuan 2020; Kisaka et al. 2020, 2022; Hirovani et al. 2022; Kin et al. 2024). Moreover, a luminosity fluctuation induced by the variability in the surrounding accretion flow is expected. Its typical duration will be the viscous timescale of the accretion flow, $t_{\text{vis}} \sim (2\pi/\alpha\Omega_{\text{K}})(R_{\text{MAD}}/H)^2 \sim 0.1\alpha_{-0.5}^{-1} \mathcal{R}_{\text{MAD},1}^{7/2} (H/0.5R_{\text{MAD}})^{-2} M_1 \text{ s}$, where $\Omega_{\text{K}} = \sqrt{GM/R_{\text{MAD}}^3}$ is the Keplerian angular velocity and H is the disk scale height. Current gamma-ray detectors, however, would not capture such a short-timescale variability. Instead, the observed luminosity would be reduced by a factor of the unknown duty cycle. Our simulation shows the oscillation cycle of $f_{\text{duty}} \sim 0.1-1$ (see

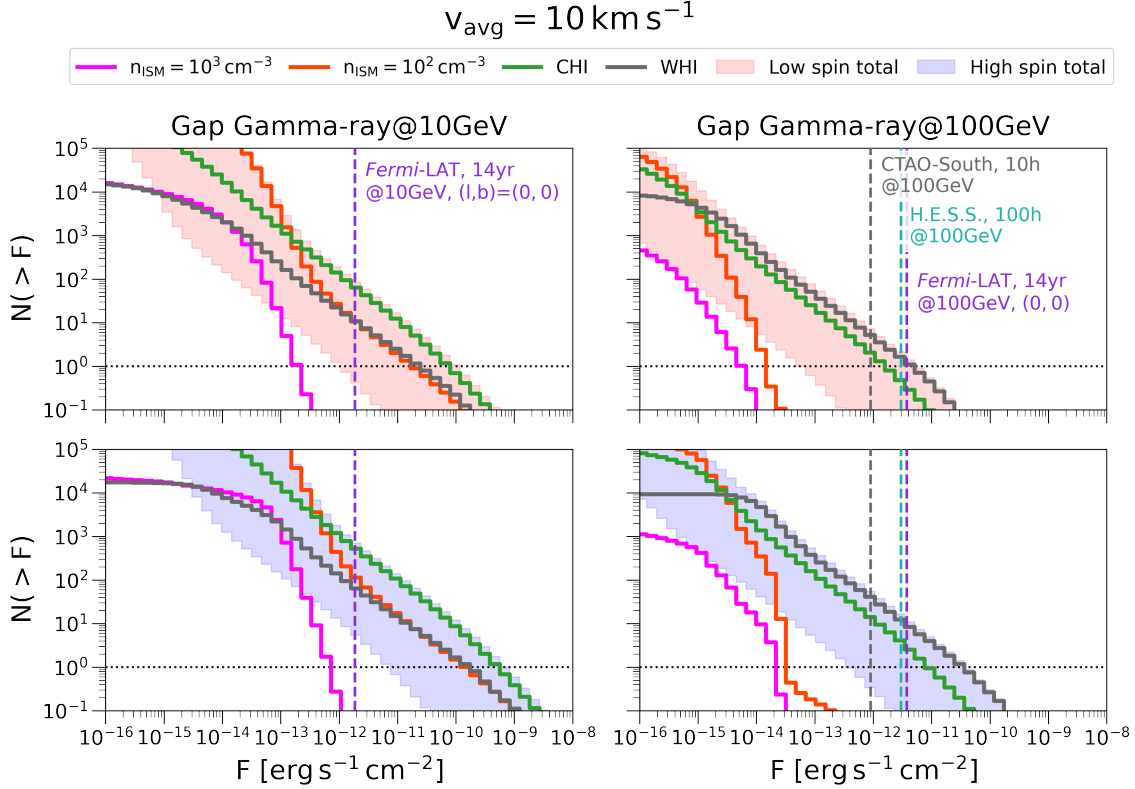


Figure 4. The cumulative distribution function of IBH gamma-ray flux, $N(>F)$, as functions of gamma-ray flux at 10 GeV (left) and at 100 GeV (right). Red and blue shaded regions denote the sums of all ISM phases for $10^{-2} \leq f_{\text{duty}} \leq 1.0$, assuming the *low spin* and the *high spin* model, respectively. Contributions of each ISM phase for $f_{\text{duty}} = 1.0$ are shown by magenta, orange, green, and gray solid lines in all panels. The sensitivity limits of *Fermi*-LAT (purple, at 10 GeV and 100 GeV, $(l, b) = (0, 0)$, 14 y; Ballet et al. (2023)), H.E.S.S. (teal, at 100 GeV, 100h; <https://www.mpi-hd.mpg.de/HESS/>), and CTAO (grey, South, 50h, at 100 GeV; <https://www.cta-observatory.org>) are also shown by thin dashed lines.

Fig. 10 in Appendix B). A naive expectation for the case of the variability produced by the accretion flow would be $f_{\text{duty}} \sim t_{\text{gap}}/t_{\text{vis}} \sim 10^{-2}$. Considering these, we multiply the factor $10^{-2} \leq f_{\text{duty}} \leq 1.0$ to the intrinsic gamma-ray flux to obtain the observed flux. We will discuss other possibilities in Section 4.3.

3. DETECTION PROSPECTS OF GAMMA-RAY EMITTING IBHS

3.1. Cumulative number & Properties for $v_{\text{avg}} = 10 \text{ km s}^{-1}$

In Fig. 4, we show the cumulative number of expected gamma-ray flux, $N(>F)$, at 10 GeV (left) and 100 GeV (right) as a function of gamma-ray flux in the case of $v_{\text{avg}} = 10 \text{ km s}^{-1}$. Here and hereafter, all the results of the detection number are normalized with $N_{\text{tot}} = 10^8$. Red and blue shaded regions in the figure represent combined values of $N(>F)$ for all ISM phases, with $10^{-2} \leq f_{\text{duty}} \leq 1$. $N(>F)$ for *high spin* model will be $N(>F) \sim 10^3$ for *Fermi*-LAT, ~ 10 for H.E.S.S., and $\sim 10^2$ for CTAO at their maximum. Depending on the value of f_{duty} , the detection by all three detectors

will be reduced by $\sim 10^{-2}$. The main contribution in all detectors will be IBHs embedded in cold and warm HI gas. IBHs in dense molecular gas clouds are rather dim, especially in the 100 GeV band. This is because MAD thermal photons for IBHs in molecular gas clouds are brighter and have peaks in higher frequency than in cold/warm HI gas due to a higher \dot{M} , leading to a stronger attenuation in ~ 100 GeV.

Next, in Fig. 5 we show the number histograms of M , d , and the galactic latitude b for IBHs with gamma-ray flux above the sensitivity limit of *Fermi*-LAT at 10 GeV ($F \approx 10^{-12} \text{ erg s}^{-1} \text{ cm}^{-2}$), H.E.S.S. ($F \approx 3.0 \times 10^{-12} \text{ erg s}^{-1} \text{ cm}^{-2}$) at 100 GeV, and CTAO ($F \approx 10^{-12} \text{ erg s}^{-1} \text{ cm}^{-2}$) at 100 GeV. The mass distributions of detectable IBHs have a bimodal shape peaking at $M \sim 5M_{\odot}$ and $\sim 40M_{\odot}$. Those peaks correspond to the preferred mass ranges to have a spectral peak at ~ 100 GeV, which are determined by a negative (positive) dependence of $E_{\gamma, \text{cur, pk}}$ ($E_{\gamma, \text{IC, pk}}$) on M (see Fig. 3). The reason for the relatively small $M \sim 40M_{\odot}$ peak for *Fermi*-LAT is that the IC component peaking around 100 GeV is more significant than the curva-

$$v_{\text{avg}} = 10 \text{ km s}^{-1}$$

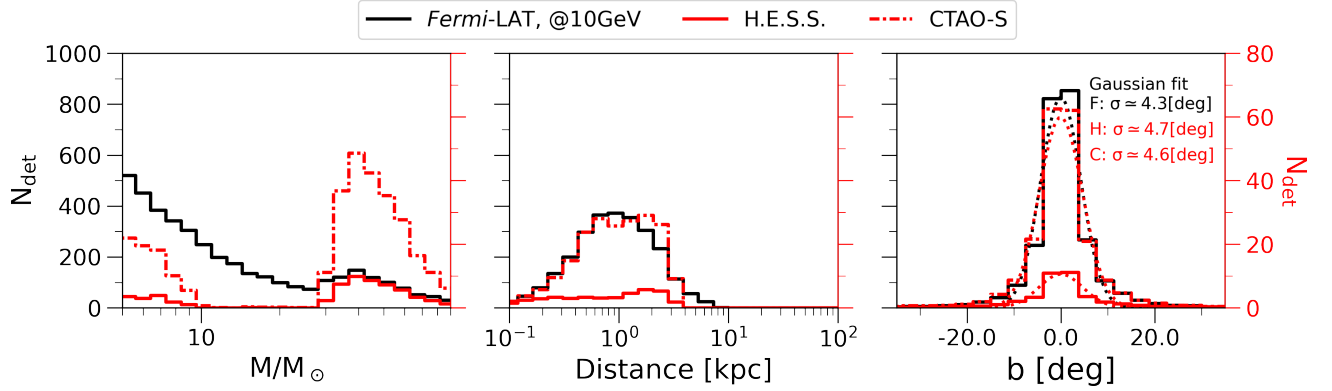


Figure 5. Histograms of M , d , and b for IBHs detectable with *Fermi*-LAT at 10 GeV (black solid), H.E.S.S. at 100 GeV (red solid), and CTAO at 100 GeV (red dash-dotted) for $v_{\text{avg}} = 10 \text{ km s}^{-1}$ and $f_{\text{duty}} = 1$. N_{det} for *Fermi*-LAT in the graph is represented on the left y-axis, while that of H.E.S.S. and CTAO are on the right red y-axis. In the 3rd panel, the results of a Gaussian fitting are shown with thin dotted lines, and the corresponding standard deviation values, σ , with texts.

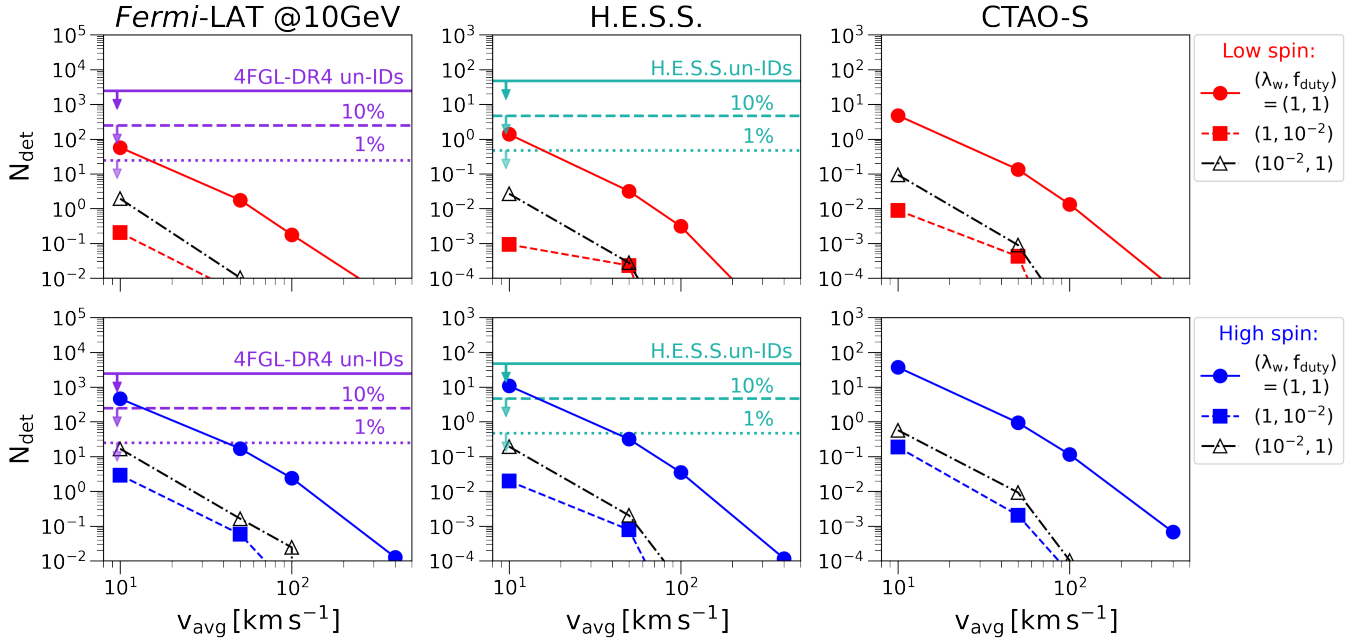


Figure 6. N_{det} above the sensitivity limits of *Fermi*-LAT (left), H.E.S.S. (middle), and CTAO (right). The top panels show the results for *low spin* and the bottom panels are for *high spin*. Results for $(\lambda_w, f_{\text{duty}}) = (1.0, 1.0)$, $(1.0, 10^{-2})$, $(10^{-2}, 1.0)$ are shown by solid lines with circles, dashed lines with square, and dash-dotted lines with triangles, respectively. Purple and teal horizontal solid/dashed/dotted lines in the left and middle panels represent the total number, 10%, and 1% of un-IDs in *Fermi*-LAT 4FGL-DR4 (Ballet et al. 2023) and H.E.S.S. Galactic plane survey (HGPS; H. E. S. S. Collaboration et al. 2018).

ture component for the majority of $M \sim 40M_{\odot}$ IBHs, and then 10 GeV flux will be reduced due to the hard spectral shape. The distance distribution peaks around $d \sim 1.0 \text{ kpc}$, which corresponds to the detection horizon for typical IBHs with the typical gamma-ray luminosity $\sim 10^{33} \text{ erg s}^{-1}$. The Galactic latitude of each detectable IBH will mainly be in $|b| \lesssim 5 \text{ deg}$, which is understood as the latitude for BHs at the typical distance $d \sim 1 \text{ kpc}$

and within the scale height of cold HI, the main contributor to the detection. This concentration to the Galactic plane is roughly consistent with that of detected un-IDs, showing a quite narrow concentration to the Galactic plane (see H. E. S. S. Collaboration et al. 2018; Abdollahi et al. 2022; Ballet et al. 2023).

3.2. Dependence on v_{avg} , f_{duty} , and λ_w

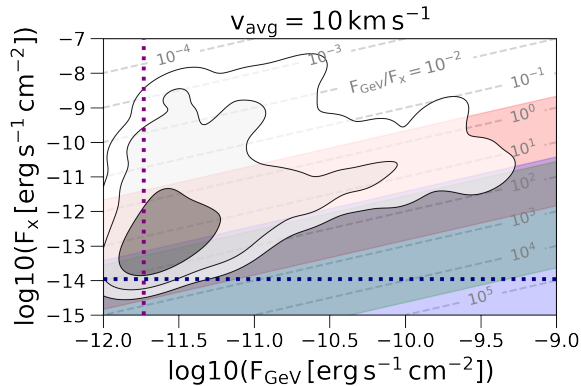


Figure 7. the σ (black), 2σ (gray), and 3σ (silver) regions that IBHs both detectable by eROSITA and *Fermi*-LAT at 10 GeV occupy in $F_{\text{GeV}}-F_X$ plane for the *low spin* case, $v_{\text{avg}} = 10 \text{ km s}^{-1}$. Differential sensitivity limits for the two detectors are shown by navy and purple dotted lines, respectively. 2σ filled region of F_{GeV}/F_X for blazers (red), milli-second pulsars (green), and young pulsars (blue) both detected by *Fermi*-LAT and eROSITA are shown for comparison (see Mayer & Becker 2024).

Fig. 6 shows the detectable IBH number above the sensitivity limit, N_{det} , for *Fermi*-LAT at 10 GeV, and H.E.S.S., CTAO at 100 GeV for various v_{avg} . For *high spin* model, $N_{\text{det}} > 1$ can be achieved for all three detectors when $v_{\text{avg}} \leq 50 \text{ km s}^{-1}$ and $f_{\text{duty}} \sim 1$. For *low spin* model, on the other hand, the number is 10^{-1} lower for all v_{avg} , and $N_{\text{det}} > 1$ by H.E.S.S. can only be achieved when $v_{\text{avg}} \sim 10 \text{ km s}^{-1}$ and $f_{\text{duty}} \sim 1$. One reason for an overall negative dependence of N_{det} on v_{avg} is that more IBHs are within the ISM scale height for the spatial distribution concentrating on the Galactic plane, which can be achieved for lower v_{avg} (see Fig. 9 in Appendix A). Also, $v \lesssim a \text{ few} \times 10 \text{ km s}^{-1}$ is preferable to achieve $\tau_0 > 30$ (see Eqs. (1) and (5)).

We show the results for $\lambda_w = 10^{-2}$ and $f_{\text{duty}} = 1$ by black dash-dotted lines with triangles in Fig. 6. Compared to the $\lambda_w = 1$ case, N_{det} is reduced by 10^{-2} for $v_{\text{avg}} \lesssim 10^2 \text{ km s}^{-1}$ and goes to zero for higher v_{avg} . We can still expect $N_{\text{det}} \sim 1-10$ for *high spin* and $f_{\text{duty}} = 1$ by *Fermi*-LAT, but ~ 0.1 by H.E.S.S. and CTAO.

4. DISCUSSIONS

4.1. Strategy for Detection

Our IBH candidates will be bright in optical, X-ray, and 10-100 GeV bands. A main strategy for the detection is thus taking cross-correlations of all-sky survey catalogs in those three bands. Kimura et al. (2021a) argued that IBH-MADs occupy similar positions to white dwarfs (WDs) in the color-magnitude (HR) diagram and the optical-X luminosity plane. By comparison, here we consider a broader range of v than Kimura et al. (2021a),

including $v \lesssim 10 \text{ km s}^{-1}$. We find that, for $\dot{m} \gtrsim 10^{-4}$, where bright gap gamma rays are emitted, intrinsic optical and X-ray luminosities will be $\times 10$ brighter and occupy a slightly bluer regime than typical WDs in the HR diagram. Dust extinction and absorption by ambient molecular gas must be considered. However, detectable ones are mainly in cold or warm HI gas, whose gas surface density is low, and hence extinction/absorption is insignificant.

Fig. 7 shows the regime that IBHs detectable in both X-ray and GeV gamma rays occupy in the $F_{\text{GeV}}-F_X$ plane. As seen from the contour, IBHs with $F_{\text{GeV}}/F_X \sim 1-10^2$ are most abundant, which is a much lower ratio than that of pulsars (blue and green). Differentiation from blazars (red), which have a similar F_{GeV}/F_X , can be done by parallax observation with *Gaia*, though careful selection of candidates will be required due to the low angular resolution of *Fermi*-LAT.

The IBH X-ray and gamma-ray flux will exhibit time-variability due to the \dot{M} fluctuation. As for the X-ray band, the flux variation with a timescale $t_{\text{vis}} \sim 0.1\alpha_{-1}^{-1} \mathcal{R}_{\text{MAD}}^{7/2} (H/0.5R_{\text{MAD}})^{-2} M_1 \text{ s}$ will be observed for nearby ones. This would be the key to distinguishing IBHs from X-ray-bright cataclysmic variables, which would have a much longer variability timescale ($\gtrsim 10 \text{ s}$, see e.g., Nishino et al. 2022). For gamma rays, only $\gg 10^3 \text{ s}$ timescale of the variability is detectable for the typical gamma-ray flux $F \sim 10^{-11} \text{ erg s}^{-1} \text{ cm}^{-2}$. Such long duration of variability will be produced by the \dot{M} fluctuation with the accretion timescale from the Bondi radius, $r_B \sim GM/v^2 \sim 5.3 \times 10^{13} M_1 (v/50 \text{ km s}^{-1})^{-2} \text{ cm}$, $t_{\text{acc}} \sim r_B/v \simeq 1.1 \times 10^7 M_1 (v/50 \text{ km s}^{-1})^{-3} \text{ s}$. The amplitude of luminosity variation will be large enough to detect ($\times 10^{\pm 2}$) due to the sensitive dependence of L_{gap} on τ_0 and the magnetospheric current amplitude (see Eq. (5), and also Kisaka et al. 2022; Kin et al. 2024). Multi-epoch observations with CTAO (or *Fermi*-LAT for nearest ones) can capture such variability.

During the interaction of IBHs and the dense ISM, a wake or filament of compressed medium with the scale of $\sim 0.1 \text{ pc}$ might be left behind (Nomura et al. 2018; Kitajima & Inutsuka 2023). Morphology analysis of ambient clouds via CO line / 21 cm line might provide another implication to the candidates' location.

A fraction of accelerated protons diffuse out of the MADs, which would interact with ambient gas to produce ultrahigh-energy gamma rays. In the case of IBHs embedded in dense molecular clouds or large-sized ($\gtrsim 100 \text{ pc}$) cold HI gas clouds, incident protons from MADs could have energy as high as $\sim \text{PeV}$, and the pp interaction rate could be high due to a high surface density of gas. Those will produce another spectral peak

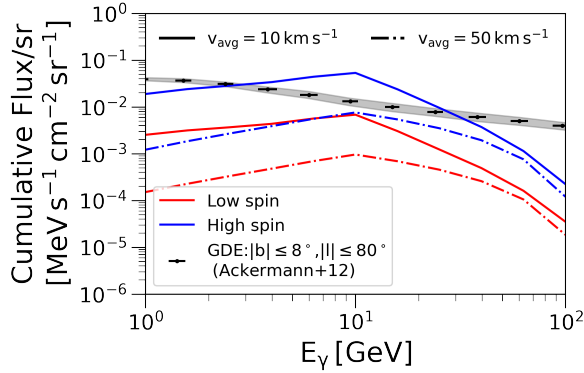


Figure 8. Plot of the combined IBH intensity spectra in 1-100 GeV for $v_{\text{avg}} = 10 \text{ km s}^{-1}$, $f_{\text{duty}} = 1.0$ (solid lines) and 50 km s^{-1} , $f_{\text{duty}} = 1.0$ (dash-dot lines).

in the 10-100 TeV band, which could explain some of LHAASO un-IDs (see Kimura et al. 2024).

4.2. Implication to BH physical parameters

The thermal synchrotron peak luminosity for gamma-ray detectable IBHs is $L_{\text{opt}} \sim 10^{34}\text{-}10^{36} \text{ erg s}^{-1}$. The peak energy, $E_{\gamma, \text{syn, pk}}$, tends to be at a few times higher energy than that of the *Gaia* band, and hence the *Gaia* band luminosity will be $\times 10^{-1}$ lower. And yet, considering their characteristic distance $d \sim 1 \text{ kpc}$ (Fig. 5), the expected *Gaia* magnitude will be $\sim 12 - 14$. *Gaia* will be able to major the parallax for such a magnitude, as long as they are in cold/warm HI gas. Some constraints on their proper motion velocity and BH mass can be obtained from the positions and movements of IBH candidates. The multi-band spectral fit and analysis of the luminosity variation would give us further information on M and \dot{M} . Also, gap gamma-ray emission will trace the dynamical behavior of the magnetosphere. Detailed analysis of the emission properties may provide observational clues to unanswered questions on the plasma dynamics in the magnetosphere.

As seen in the leftmost panel of Fig. 5, H.E.S.S. and CTAO preferably detect massive ($M \gtrsim 30M_{\odot}$) BHs. So far, a few tens of BHs with $M \sim 30M_{\odot}$ have been found through the gravitational wave observation, and also *Gaia* astrometrical analysis (Gaia BH3). Their origins remain unclear, though several possibilities are proposed including very massive stars formed in zero/low-metal environment (e.g., Kinugawa et al. 2014; Tanikawa et al. 2022) and hierarchical mergers in dense star clusters (e.g., Kumamoto et al. 2020; Tagawa et al. 2020). If we find several IBH candidates using gamma-ray detectors, estimates of the mass and dynamical motion of IBH candidates might achieve important suggestions on their formation channel.

The *high spin* model with $v_{\text{avg}} \lesssim 10^2 \text{ km s}^{-1}$ predicts N_{det} comparable to the $\sim 10\%$ of *Fermi*-LAT un-IDs (see Fig. 6). Considering the rarity of hard spectral objects in *Fermi*-LAT un-IDs (Abdollahi et al. 2022; Yang et al. 2023; Zhu et al. 2024), our results may suggest that $v_{\text{avg}} > 10 \text{ km s}^{-1}$ and low spin values are preferred not to overshoot the current un-ID number.

The contribution of IBHs below the detection limit to the Galactic gamma-ray diffuse emission (GDE) would be non-negligible. We demonstrate 1-100 GeV combined photon intensities for several parameters in Fig. 8. Here, we combine BHs inside $|b| \leq 8^{\circ}$ and $|l| \leq 80^{\circ}$ with their radiation flux below the sensitivity threshold of *Fermi*-LAT, and divide them with corresponding area $\Pi \sim 0.78 \text{ sr}$. All models peak at $\sim 10 \text{ GeV}$, reflecting the characteristic peak of individual spectra. We obtain the intensity reaching a fraction ($\sim 50\%$ at most) of GDE flux for $v_{\text{avg}} = 50 \text{ km s}^{-1}$. The intensity for *high spin* and $v_{\text{avg}} = 10 \text{ km s}^{-1}$ case with $f_{\text{duty}} = 1$ exceeds the observed GDE intensity, which might also put a constraint on the spin value and v_{avg} . Koshimoto et al. (2024) discussed influence of v_{avg} on the detectability of microlensing events induced by IBHs. They concluded that $v_{\text{avg}} \lesssim 10^2 \text{ km s}^{-1}$ is preferred to explain the detection of OGLE-2011-BLG-0462, a singular example of the IBH microlensing event. Combining with our results, $v_{\text{avg}} \sim \text{a few} \times 10 \text{ km s}^{-1}$ might be a suitable value for the average kick velocity, which is also consistent with the best-fit transverse motion velocity of the IBH responsible for OGLE-2011-BLG-0462 event in Lam & Lu ($v \sim 37.6 \text{ km s}^{-1}$; 2023).

Above discussion depends on the assumption of λ_w and f_{duty} : we obtain $\times 10^{-2}$ lower N_{det} for $\lambda_w = 10^{-2}$ or $f_{\text{duty}} = 10^{-2}$, regardless of v_{avg} and the distribution of a (Fig. 6). In this case, we hardly achieve any constraints on v_{avg} and a from the detection number or their contribution to GDE. Recent 3D GRMHD simulations of BHL accretion show $\lambda_w \sim 0.1\text{-}0.5$ (Kaaz et al. 2023; Galishnikova et al. 2024; Kim & Most 2024), and thus our fiducial value $\lambda_w = 1$ might overestimate \dot{M} . About 10^{-1} reduction in N_{det} is expected for $\lambda_w \sim 0.1$. *Fermi*-LAT can still detect $\sim 10\text{-}100$ for $v_{\text{avg}} = 10 \text{ km s}^{-1}$ and *high spin*, which corresponds to $\sim 1\text{-}10\%$ of un-IDs.

4.3. Caveats

Previous attempts to estimate N_{tot} have yielded a variety of values ranging $10^8\text{-}10^9$, depending on the model for the star-formation history and the stellar evolution (e.g. van den Heuvel 1992; Brown & Bethe 1994; Timmes et al. 1996; Caputo et al. 2017; Olejak et al. 2020). The detectable IBH number is proportional to N_{tot} , and then we would expect $\times 10$ higher N_{det} for all parameters

with $N_{\text{tot}} = 10^9$, which would give tighter constraints on v_{avg} and a , as discussed in Section 4.2. The IBH mass function remains uncertain as well. For a harder (softer) power-law index or a higher (lower) maximum mass than our assumptions, the higher (lower) N_{det} is expected. Its effect would be more eminent in observations at ~ 100 GeV than at ~ 10 GeV, since those detect more $M > 10M_{\odot}$ IBHs (see Fig. 5). On the contrary, if the minimum mass is lower (higher) than our assumption, N_{det} at ~ 10 GeV would increase (decrease) because the higher the mass is, the lower $E_{\gamma, \text{cur, pk}}$ becomes, and vice versa.

Some uncertainties in the gap dynamics must be noted: One is the position of the gap. We have assumed the spherical distribution of the gap around the BH and isotropic gamma-ray emission. The attenuation by MAD soft photons and Thomson scatterings of accreting plasma is insignificant for 10-100 GeV gap main emission due to low photon/particle number density. Thus, the radiated photon could escape from the system all over the direction. In several BH magnetosphere 1D GRPIC simulations (Kisaka et al. 2020; Chen & Yuan 2020; Kisaka et al. 2022; Kin et al. 2024), a spark gap opens around the null surface, which is almost spherical for the split-monopole field geometry (see Hirovani & Pu 2016). The monopole-like shape of the magnetic field near the horizon is observed in GRMHD simulations (see Tchekhovskoy et al. 2010; Ripperda et al. 2022), and therefore the sphericity of the gap might be valid, leading to the isotropic gamma-ray emissions. In contrast, recent 2D GRPIC simulations of the BH magnetosphere (e.g. Crinquand et al. 2020) observed the gap opening mainly around the polar region. If the gap opening angle is limited, our expectation of the detection number will be reduced. Such qualitative differences in behaviors of the magnetosphere between local 1D and global 2D simulations need to be addressed in the future.

The gap duty cycle is also worth investigating because, as shown above, the reduction in the persistent gamma-ray luminosity significantly affects the number of detections. Other than two characteristic timescales that we mention in Section 2.7, the sporadic magnetic reconnection in the equatorial plane will change the global structure of the electric current in the magnetosphere, which might produce a cyclic behavior on the gap activity (see Vos et al. 2024). The pair cascading might also be induced by this sudden magnetic energy release (Kimura et al. 2022; Chen et al. 2023; Hakobyan et al. 2023). The amount of injected pair could be large enough to screen the entire magnetosphere, but due to a much longer interval between the flare ($t_{\text{int}} \sim 10^3 r_g/c$, see Ripperda et al. 2022) compared to the approximated escape

timescale of the injected plasma, $t_{\text{esc}} \sim 3R_{\text{MAD}}/c \sim 30r_g/c$, the gap might become active again in between the flares. A simple estimate for the duty cycle will be $f_{\text{duty}} \sim (t_{\text{int}} - t_{\text{esc}})/t_{\text{int}} \sim 1$, but a detailed simulation focusing on such the concordance between the magnetosphere and the accretion flow will be required to investigate the precise behavior.

5. CONCLUSIONS

In this work, we have investigated the prospect of detecting IBHs through high-energy gamma rays from magnetospheric gaps. We calculate the spatial distribution and the proper motion velocity of IBH samples following the method described in Tsuna et al. (2018); Tsuna & Kawanaka (2019). We then evaluated the mass accretion rate of each IBH and calculated multi-wavelength radiation flux from their MADs. Gap gamma-ray flux can be calculated using radiation properties of optical soft photons from the MAD and the dependence of $\gamma_{e, \text{max}}$, $L_{\text{cur, pk}}$, and $L_{\text{IC, pk}}$ on τ_0 , which obtained from our simulations. Gap gamma rays can be bright if IBHs are embedded in relatively dense ISM, for which $\dot{m} \gtrsim 10^{-4}$. In the case of $v_{\text{avg}} = 10 \text{ km s}^{-1}$, the *Fermi*-LAT un-IDs would contain $\sim 10^3$ of gamma-ray emitting IBHs, and for H.E.S.S., there would be ~ 10 objects near the Galactic plane, at maximum (see Fig. 6). Future observation by CTAO would detect $\lesssim 10^2$ candidates near the Galactic plane, mainly in cold/warm HI gas. Optical and X-ray emissions from surrounding MADs are expected as counterparts. A strong time variation in the gamma-ray luminosity is expected, due to a fluctuation in the mass accretion rate, which can be detected through the observation by *Fermi*-LAT or CTAO with $\sim 10^3$ s operation time. Those IBHs could also contribute to the GDE, mainly in $\sim \text{GeV}$. Constraints on the supernova kick velocity and the BH spin could be achieved by comparison with the number of existing un-IDs or observed GDE intensity.

1 Numerical computations were carried out on Cray
 2 XC50, PC cluster, Small Parallel Computers, and anal-
 3 ysis servers at the Center for Computational Astro-
 4 physics, National Astronomical Observatory of Japan,
 5 and Yukawa-21 at Yukawa Institute for Theoretical
 6 Physics at Kyoto University. K.K. thanks Ryunosuke
 7 Maeda for practical advice on the computation in this
 8 work. This work was supported by the Graduate Pro-
 9 gram on Physics for the Universe (GP-PU), Tohoku
 10 University (K.K.), JST SPRING, Grant Number JP-
 11 MJSP2114 (K.K., R.K.), KAKENHI No. 22K14028
 12 (S.S.K.), 21H04487 (S.S.K.), 23H04899 (S.S.K). S.S.K.
 13 acknowledges the support of the Tohoku Initiative for
 14 Fostering Global Researchers for Interdisciplinary Sci-
 15 ences (TI-FRIS) of MEXT's Strategic Professional De-
 16 velopment Program for Young Researchers.

APPENDIX

A. IBH DYNAMICAL CALCULATION RESULTS

Our IBH dynamical calculation follows the methods described in Tsuna et al. (2018); Tsuna & Kawanaka (2019). The total number of BH particles is 10^5 , which is $\times 10$ smaller than in Tsuna et al. (2018). We set the numerical integration time-step as $\Delta t = 10^3$ yr (equivalent to 10^7 divisions of 10 Gyr) for BHs at $r > 10$ pc, which is shorter/comparable to their dynamical timescale. For BHs at $r \leq 10$ pc, we use the 1/100 shorter time step $\Delta t = 10$ yr to achieve enough time resolutions. With our fixed time step treatment, some of IBHs could have artificially high velocity. To reduce the number of such IBHs, we introduce the smoothing terms to the equation of motion of BHs (Eqs. (9) and (10) of Tsuna et al. (2018)):

$$\begin{aligned} \frac{dv_R}{dt} &= \frac{v_\theta^2}{\sqrt{R^2 + \epsilon_1^2}} - \sum_{i=1,2} \frac{GM_i R}{\{R^2 + [a_i + (z^2 + b_i^2)^{1/2}]^2 + \epsilon_2^2\}^{3/2}} - \frac{GM_h}{R_h} \frac{R}{\sqrt{R^2 + \epsilon_i^2}} \left[\frac{R_h}{\sqrt{R^2 + \epsilon_i^2} \sqrt{R^2 + R_h^2 + \epsilon_2^2}} \right], \\ \frac{dv_z}{dt} &= - \sum_{i=1,2} \frac{GM_i z [a_i + \sqrt{z^2 + b_i^2}]}{\{R^2 + [a_i + \sqrt{z^2 + b_i^2}]^2 + \epsilon_2^2\}^{3/2} \sqrt{z^2 + b_i^2}} - \frac{GM_h}{R_h} \frac{R}{\sqrt{R^2 + \epsilon_i^2}} \left[\frac{R_h}{\sqrt{R^2 + \epsilon_i^2} \sqrt{R^2 + R_h^2 + \epsilon_2^2}} \right], \end{aligned} \quad (\text{A1})$$

where v_R, v_θ, v_z is the R, θ, z velocity components of BH particles. $M_i = \{4.07 \times 10^9 M_\odot, 6.58 \times 10^{10} M_\odot\}$, $a_i = \{0, 4.85 \text{ kpc}\}$, $b_i = \{0.184 \text{ kpc}, 0.305 \text{ kpc}\}$ ($i = 1, 2$), $M_h = 1.62 \times 10^{12} M_\odot$, and $R_h = 200 \text{ kpc}$ is the values of the constants obtained from Irrgang et al. (2013). We set $(\epsilon_1, \epsilon_2) = (0.1 \text{ pc}, 1.0 \text{ pc})$ when BHs are at $r = (R^2 + z^2)^{1/2} \leq 10 \text{ pc}$ during the calculation and $(0.1 \text{ pc}, 10 \text{ pc})$ when they are at $r > 10 \text{ pc}$. We have checked the number of BHs having the unphysical velocity $v = (v_R^2 + v_\theta^2 + v_z^2)^{1/2} > v_{\text{esc}}(r = 10 \text{ pc}) \simeq 700 \text{ km s}^{-1}$ are fewer than 0.1% of the total for such ϵ_1, ϵ_2 , which is negligible in overall detectability calculations.

We show results of IBH dynamical calculations for 4 different values of v_{avg} in Fig. 9. Their spatial distribution approaches from the initial exponential disk shape to a more spherical shape for higher v_{avg} , consistent with Tsuna et al. (2018). The velocity distribution peaks at $v \sim v_{\text{avg}}$. The absence of low velocity ($v \lesssim 10 \text{ km s}^{-1}$) BHs in $v_{\text{avg}} \geq 100 \text{ km s}^{-1}$ is the consequence of the limited number of IBH particles, which might reduce the resultant number of detectable IBHs.

B. THE SUMMARY OF SUPPLEMENTAL ANALYSIS OF THE SPARK GAP DYNAMICAL DEPENDENCE ON THE BH SPIN

We hereby summarize our supplemental analysis of the dependence of the spark gap dynamics on the BH spin. We use the 1D GRPIC simulation code Zeltron (Levinson & Cerutti 2018). We choose the same parameter sets for the

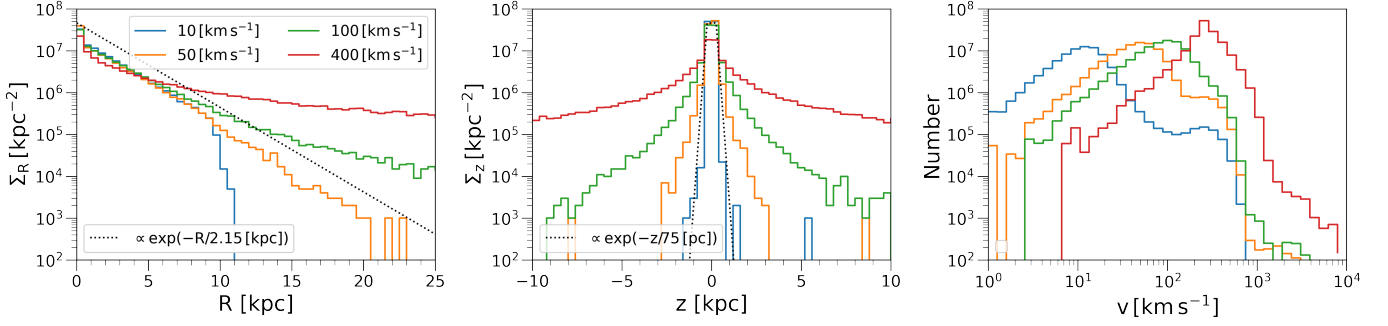


Figure 9. Dynamical calculation results of the surface density in R direction (left), the surface density in z direction (middle), and the velocity distribution (right). The black dotted line in each panel represents the initial spatial/velocity distributions.

system as Kin et al. (2024): BH mass $M = 10M_{\odot}$, the magnetic field at the horizon $B_H = 2\pi \times 10^7$ G, $\theta = 30^\circ$, and the characteristic energy of the soft photon fields $\epsilon_{\min} = 10^{-6}$. We change the dimensionless spin parameter $a = 0.1, 0.5$ and compare the results with $a = 0.9$ runs on Kin et al. (2024). For each spin value, we perform the run with three different values of fiducial optical depth $\tau_0 = 30, 100, 300$ to investigate the dynamical difference quantitatively. The initial number of the particles per cell (PPC) is set as 45, which is the same value for Kisaka et al. (2022); Kin et al. (2024). We also conducted runs for $a = 0.1, 0.5$ and $\tau_0 = 30$ with a 3 times higher PPC, 135 (not in the figure), and checked that they reached their convergence.

Fig. 10 shows results from our simulation. Similar to $a = 0.9$ cases, we observe the spark gap intermittently opens around the null surface. This behavior is the result of the intermittent secondary pair production induced by the particle acceleration in the gap: particles accelerated in the gap up-scatter soft photons, which soon annihilate with other soft photons to produce electron-positron pairs. Those secondary-produced pairs will compensate for the charge/current deficiency, and then after some time, the gap longitudinal electric field will be screened out. The pair multiplicity in the gap affects the physical extension and the peak amplitude of the gap electric field, and as a result, $\gamma_{e,\max}$, $L_{\text{cur,pk}}$ is sensitive to τ_0 . $L_{\text{IC,pk}}$ is less sensitive to τ_0 than $L_{\text{cur,pk}}$ because (1) the persistent flow of plasma particles just outside of the gap is required to maintain the steady electric current, whose amplitude is independent to τ_0 , and then those particles will produce a steady flux of IC scattered photons, and (2) scatterings in the gap mainly occurs in the KN regime, in which IC emitting power is weakly dependent to the particle Lorentz factor γ_e . We obtain the averaged fitting function of those parameters: $\gamma_{e,\max} \approx 8.9 \times 10^6 (\tau_0/30)^{-0.4}$, $L_{\text{cur,pk}} \approx 10^{-2} (\tau_0/30)^{-2.8} L_{\text{BZ}}$, and $L_{\text{IC,pk}} \approx 5.8 \times 10^{-4} L_{\text{BZ}} \propto \tau_0^{-0.2}$ (black dashed lines in the figure). $L_{\text{cur,pk}}/L_{\text{BZ}}$ and $L_{\text{IC,pk}}/L_{\text{BZ}}$ have a weak dependence on the BH spin. For simplicity, we assume that they are independent of a in the context. The factor 3-10 difference of $L_{\text{cur,pk}}/L_{\text{BZ}}$, $L_{\text{IC,pk}}/L_{\text{BZ}}$ may result from the slightly larger size of the gap (top left panel of Fig. 10) leading to the larger amplitude of the gap electric field (see Eq. (12) of Kin et al. 2024, for a reference), and also the weaker gravitational redshift effect for the lower spin value.

REFERENCES

- Abbott, R., Abbott, T. D., Acernese, F., et al. 2023, Physical Review X, 13, 011048, doi: [10.1103/PhysRevX.13.011048](https://doi.org/10.1103/PhysRevX.13.011048)
- Abdollahi, S., Acero, F., Baldini, L., et al. 2022, ApJS, 260, 53, doi: [10.3847/1538-4365/ac6751](https://doi.org/10.3847/1538-4365/ac6751)
- Agol, E., & Kamionkowski, M. 2002, MNRAS, 334, 553, doi: [10.1046/j.1365-8711.2002.05523.x](https://doi.org/10.1046/j.1365-8711.2002.05523.x)
- Aharonian, F., Akhperjanian, A. G., Bazer-Bachi, A. R., et al. 2006, A&A, 457, 899, doi: [10.1051/0004-6361:20065351](https://doi.org/10.1051/0004-6361:20065351)
- Atwood, W. B., Abdo, A. A., Ackermann, M., et al. 2009, ApJ, 697, 1071, doi: [10.1088/0004-637X/697/2/1071](https://doi.org/10.1088/0004-637X/697/2/1071)
- Ballet, J., Bruel, P., Burnett, T. H., Lott, B., & The Fermi-LAT collaboration. 2023, arXiv e-prints, arXiv:2307.12546, doi: [10.48550/arXiv.2307.12546](https://doi.org/10.48550/arXiv.2307.12546)
- Barkov, M. V., Khangulyan, D. V., & Popov, S. B. 2012, MNRAS, 427, 589, doi: [10.1111/j.1365-2966.2012.22029.x](https://doi.org/10.1111/j.1365-2966.2012.22029.x)
- Bland-Hawthorn, J., & Reynolds, R. 2000, in Encyclopedia of Astronomy and Astrophysics, ed. P. Murdin, 2636, doi: [10.1888/0333750888/2636](https://doi.org/10.1888/0333750888/2636)
- Blandford, R. D., & Znajek, R. L. 1977, MNRAS, 179, 433, doi: [10.1093/mnras/179.3.433](https://doi.org/10.1093/mnras/179.3.433)
- Brown, G. E., & Bethe, H. A. 1994, ApJ, 423, 659, doi: [10.1086/173844](https://doi.org/10.1086/173844)

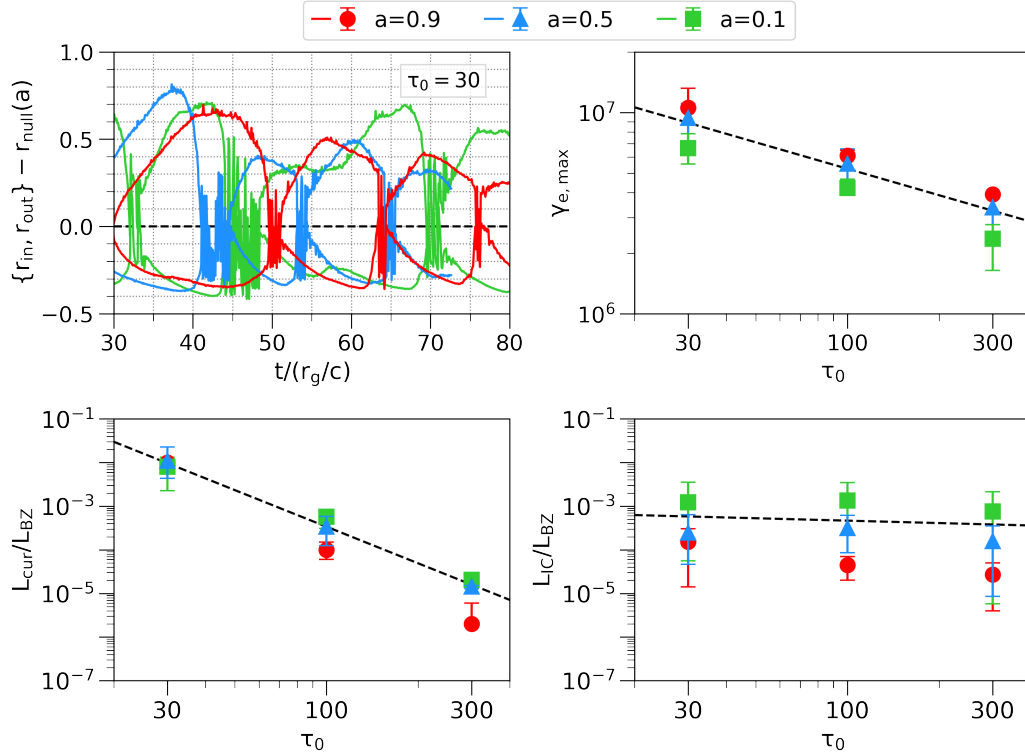


Figure 10. Results from our simulation. The results for $a = 0.9$ ('LA1', 'LA3', and 'LA5' model in Kin et al. 2024) are shown with red curves/dots for comparison. Each panel shows (top left) the time evolution of spark gap inner/outer radius $r_{in/out}$ around the null r_{null} for $\tau_0 = 30$, $\gamma_{e,max}$ (top right), $L_{cur,pk}$ (bottom left), and $L_{IC,pk}$ (bottom right) as functions of τ_0 and the power-law fitted curves for each parameter (black dashed lines, see the context), respectively.

- Cao, X. 2011, *ApJ*, 737, 94,
doi: [10.1088/0004-637X/737/2/94](https://doi.org/10.1088/0004-637X/737/2/94)
- Caputo, D. P., de Vries, N., Patruno, A., & Portegies Zwart, S. 2017, *MNRAS*, 468, 4000, doi: [10.1093/mnras/stw3336](https://doi.org/10.1093/mnras/stw3336)
- Chael, A., Rowan, M., Narayan, R., Johnson, M., & Sironi, L. 2018, *MNRAS*, 478, 5209, doi: [10.1093/mnras/sty1261](https://doi.org/10.1093/mnras/sty1261)
- Chen, A. Y., Uzdensky, D., & Dexter, J. 2023, *ApJ*, 944, 173, doi: [10.3847/1538-4357/acb68a](https://doi.org/10.3847/1538-4357/acb68a)
- Chen, A. Y., & Yuan, Y. 2020, *ApJ*, 895, 121,
doi: [10.3847/1538-4357/ab8c46](https://doi.org/10.3847/1538-4357/ab8c46)
- Cherenkov Telescope Array Consortium, Acharya, B. S., Agudo, I., et al. 2019, *Science with the Cherenkov Telescope Array*, doi: [10.1142/10986](https://doi.org/10.1142/10986)
- Coppi, P. S., & Blandford, R. D. 1990, *MNRAS*, 245, 453,
doi: [10.1093/mnras/245.3.453](https://doi.org/10.1093/mnras/245.3.453)
- Corral-Santana, J. M., Casares, J., Muñoz-Darias, T., et al. 2016, *A&A*, 587, A61, doi: [10.1051/0004-6361/201527130](https://doi.org/10.1051/0004-6361/201527130)
- Crinquand, B., Cerutti, B., Philippov, A., Parfrey, K., & Dubus, G. 2020, *PhRvL*, 124, 145101,
doi: [10.1103/PhysRevLett.124.145101](https://doi.org/10.1103/PhysRevLett.124.145101)
- Draghis, P. A., Miller, J. M., Costantini, E., et al. 2024, *ApJ*, 969, 40, doi: [10.3847/1538-4357/ad43ea](https://doi.org/10.3847/1538-4357/ad43ea)
- Edgar, R. 2004, *NewAR*, 48, 843,
doi: [10.1016/j.newar.2004.06.001](https://doi.org/10.1016/j.newar.2004.06.001)
- El-Badry, K., Rix, H.-W., Quataert, E., et al. 2023a, *MNRAS*, 518, 1057, doi: [10.1093/mnras/stac3140](https://doi.org/10.1093/mnras/stac3140)
- El-Badry, K., Rix, H.-W., Cendes, Y., et al. 2023b, *MNRAS*, 521, 4323, doi: [10.1093/mnras/stad799](https://doi.org/10.1093/mnras/stad799)
- Fender, R. P., Maccarone, T. J., & Heywood, I. 2013, *MNRAS*, 430, 1538, doi: [10.1093/mnras/sts688](https://doi.org/10.1093/mnras/sts688)
- Fujita, Y., Inoue, S., Nakamura, T., Manmoto, T., & Nakamura, K. E. 1998, *ApJL*, 495, L85,
doi: [10.1086/311220](https://doi.org/10.1086/311220)
- Gaia Collaboration, Panuzzo, P., Mazeh, T., et al. 2024, *A&A*, 686, L2, doi: [10.1051/0004-6361/202449763](https://doi.org/10.1051/0004-6361/202449763)
- Galishnikova, A., Philippov, A., Quataert, E., Chatterjee, K., & Liska, M. 2024, arXiv e-prints, arXiv:2409.11486,
doi: [10.48550/arXiv.2409.11486](https://doi.org/10.48550/arXiv.2409.11486)
- H. E. S. S. Collaboration, Abdalla, H., Abramowski, A., et al. 2018, *A&A*, 612, A1,
doi: [10.1051/0004-6361/201732098](https://doi.org/10.1051/0004-6361/201732098)
- Hakobyan, H., Ripperda, B., & Philippov, A. A. 2023, *ApJL*, 943, L29, doi: [10.3847/2041-8213/acb264](https://doi.org/10.3847/2041-8213/acb264)
- Hirotoni, K., & Pu, H.-Y. 2016, *ApJ*, 818, 50,
doi: [10.3847/0004-637X/818/1/50](https://doi.org/10.3847/0004-637X/818/1/50)

- Hirotani, K., Pu, H.-Y., Outmani, S., et al. 2018, *ApJ*, 867, 120, doi: [10.3847/1538-4357/aae47a](https://doi.org/10.3847/1538-4357/aae47a)
- Hirotani, K., Shang, H., Krasnopolsky, R., & Nishikawa, K.-i. 2022, arXiv e-prints, arXiv:2209.13140. <https://arxiv.org/abs/2209.13140>
- Ichimaru, S. 1977, *ApJ*, 214, 840, doi: [10.1086/155314](https://doi.org/10.1086/155314)
- Ioka, K., Matsumoto, T., Teraki, Y., Kashiyama, K., & Murase, K. 2017, *MNRAS*, 470, 3332, doi: [10.1093/mnras/stx1337](https://doi.org/10.1093/mnras/stx1337)
- Irrgang, A., Wilcox, B., Tucker, E., & Schiefelbein, L. 2013, *A&A*, 549, A137, doi: [10.1051/0004-6361/201220540](https://doi.org/10.1051/0004-6361/201220540)
- Kaaz, N., Murguia-Berthier, A., Chatterjee, K., Liska, M. T. P., & Tchekhovskoy, A. 2023, *ApJ*, 950, 31, doi: [10.3847/1538-4357/acc7a1](https://doi.org/10.3847/1538-4357/acc7a1)
- Kim, Y., & Most, E. R. 2024, arXiv e-prints, arXiv:2409.12359, doi: [10.48550/arXiv.2409.12359](https://doi.org/10.48550/arXiv.2409.12359)
- Kimura, S. S., Kashiyama, K., & Hotokezaka, K. 2021a, *ApJL*, 922, L15, doi: [10.3847/2041-8213/ac35dc](https://doi.org/10.3847/2041-8213/ac35dc)
- Kimura, S. S., Sudoh, T., Kashiyama, K., & Kawanaka, N. 2021b, *ApJ*, 915, 31, doi: [10.3847/1538-4357/abff58](https://doi.org/10.3847/1538-4357/abff58)
- Kimura, S. S., & Toma, K. 2020, *ApJ*, 905, 178, doi: [10.3847/1538-4357/abc343](https://doi.org/10.3847/1538-4357/abc343)
- Kimura, S. S., Toma, K., Noda, H., & Hada, K. 2022, *ApJL*, 937, L34, doi: [10.3847/2041-8213/ac8d5a](https://doi.org/10.3847/2041-8213/ac8d5a)
- Kimura, S. S., Tomida, K., Kobayashi, M. I. N., Kin, K., & Zhang, B. 2024, arXiv e-prints, arXiv:2412.08136, doi: [10.48550/arXiv.2412.08136](https://doi.org/10.48550/arXiv.2412.08136)
- Kin, K., Kisaka, S., Toma, K., Kimura, S. S., & Levinson, A. 2024, *ApJ*, 964, 78, doi: [10.3847/1538-4357/ad20cd](https://doi.org/10.3847/1538-4357/ad20cd)
- Kinugawa, T., Inayoshi, K., Hotokezaka, K., Nakauchi, D., & Nakamura, T. 2014, *MNRAS*, 442, 2963, doi: [10.1093/mnras/stu1022](https://doi.org/10.1093/mnras/stu1022)
- Kisaka, S., Levinson, A., & Toma, K. 2020, *ApJ*, 902, 80, doi: [10.3847/1538-4357/abb46c](https://doi.org/10.3847/1538-4357/abb46c)
- Kisaka, S., Levinson, A., Toma, K., & Niv, I. 2022, *ApJ*, 924, 28, doi: [10.3847/1538-4357/ac35da](https://doi.org/10.3847/1538-4357/ac35da)
- Kitajima, K., & Inutsuka, S.-i. 2023, *ApJ*, 945, 39, doi: [10.3847/1538-4357/acb7ea](https://doi.org/10.3847/1538-4357/acb7ea)
- Koshimoto, N., Kawanaka, N., & Tsuna, D. 2024, arXiv e-prints, arXiv:2405.07502, doi: [10.48550/arXiv.2405.07502](https://doi.org/10.48550/arXiv.2405.07502)
- Kumamoto, J., Fujii, M. S., & Tanikawa, A. 2020, *MNRAS*, 495, 4268, doi: [10.1093/mnras/staa1440](https://doi.org/10.1093/mnras/staa1440)
- Kuze, R., Kimura, S. S., & Toma, K. 2022, *ApJ*, 935, 159, doi: [10.3847/1538-4357/ac7ec1](https://doi.org/10.3847/1538-4357/ac7ec1)
- . 2024, *ApJ*, 977, 22, doi: [10.3847/1538-4357/ad88f4](https://doi.org/10.3847/1538-4357/ad88f4)
- Kwan, T. M., Dai, L., & Tchekhovskoy, A. 2023, *ApJL*, 946, L42, doi: [10.3847/2041-8213/acc334](https://doi.org/10.3847/2041-8213/acc334)
- Lam, C. Y., & Lu, J. R. 2023, *ApJ*, 955, 116, doi: [10.3847/1538-4357/aced4a](https://doi.org/10.3847/1538-4357/aced4a)
- Lam, C. Y., Lu, J. R., Udalski, A., et al. 2022, *ApJL*, 933, L23, doi: [10.3847/2041-8213/ac7442](https://doi.org/10.3847/2041-8213/ac7442)
- Levinson, A., & Cerutti, B. 2018, *A&A*, 616, A184, doi: [10.1051/0004-6361/201832915](https://doi.org/10.1051/0004-6361/201832915)
- Levinson, A., & Rieger, F. 2011, *ApJ*, 730, 123, doi: [10.1088/0004-637X/730/2/123](https://doi.org/10.1088/0004-637X/730/2/123)
- Mahadevan, R. 1997, *ApJ*, 477, 585, doi: [10.1086/303727](https://doi.org/10.1086/303727)
- Mayer, M. G. F., & Becker, W. 2024, *A&A*, 684, A208, doi: [10.1051/0004-6361/202348620](https://doi.org/10.1051/0004-6361/202348620)
- Nagarajan, P., & El-Badry, K. 2024, arXiv e-prints, arXiv:2411.16847, doi: [10.48550/arXiv.2411.16847](https://doi.org/10.48550/arXiv.2411.16847)
- Narayan, R., Igumenshchev, I. V., & Abramowicz, M. A. 2003, *PASJ*, 55, L69, doi: [10.1093/pasj/55.6.L69](https://doi.org/10.1093/pasj/55.6.L69)
- Narayan, R., Sądowski, A., Penna, R. F., & Kulkarni, A. K. 2012, *MNRAS*, 426, 3241, doi: [10.1111/j.1365-2966.2012.22002.x](https://doi.org/10.1111/j.1365-2966.2012.22002.x)
- Narayan, R., & Yi, I. 1994, *ApJL*, 428, L13, doi: [10.1086/187381](https://doi.org/10.1086/187381)
- Nishino, Y., Kimura, M., Sako, S., et al. 2022, *PASJ*, 74, L17, doi: [10.1093/pasj/psac027](https://doi.org/10.1093/pasj/psac027)
- Nomura, M., Oka, T., Yamada, M., et al. 2018, *ApJ*, 859, 29, doi: [10.3847/1538-4357/aabe32](https://doi.org/10.3847/1538-4357/aabe32)
- Olejak, A., Belczynski, K., Bulik, T., & Sobolewska, M. 2020, *A&A*, 638, A94, doi: [10.1051/0004-6361/201936557](https://doi.org/10.1051/0004-6361/201936557)
- Repetto, S., Igoshev, A. P., & Nelemans, G. 2017, *MNRAS*, 467, 298, doi: [10.1093/mnras/stx027](https://doi.org/10.1093/mnras/stx027)
- Ripperda, B., Liska, M., Chatterjee, K., et al. 2022, *ApJL*, 924, L32, doi: [10.3847/2041-8213/ac46a1](https://doi.org/10.3847/2041-8213/ac46a1)
- Rowan, M. E., Sironi, L., & Narayan, R. 2017, *ApJ*, 850, 29, doi: [10.3847/1538-4357/aa9380](https://doi.org/10.3847/1538-4357/aa9380)
- Sahu, K. C., Anderson, J., Casertano, S., et al. 2022, *ApJ*, 933, 83, doi: [10.3847/1538-4357/ac739e](https://doi.org/10.3847/1538-4357/ac739e)
- Shakura, N. I., & Sunyaev, R. A. 1973, *A&A*, 24, 337
- Shapiro, S. L., & Lightman, A. P. 1976, *ApJ*, 204, 555, doi: [10.1086/154203](https://doi.org/10.1086/154203)
- Shapiro, S. L., & Teukolsky, S. A. 1986, *Black Holes, White Dwarfs and Neutron Stars: The Physics of Compact Objects*
- Tagawa, H., Haiman, Z., & Kocsis, B. 2020, *ApJ*, 892, 36, doi: [10.3847/1538-4357/ab7922](https://doi.org/10.3847/1538-4357/ab7922)
- Tanikawa, A., Yoshida, T., Kinugawa, T., et al. 2022, *ApJ*, 926, 83, doi: [10.3847/1538-4357/ac4247](https://doi.org/10.3847/1538-4357/ac4247)
- Tchekhovskoy, A., Narayan, R., & McKinney, J. C. 2010, *ApJ*, 711, 50, doi: [10.1088/0004-637X/711/1/50](https://doi.org/10.1088/0004-637X/711/1/50)
- . 2011, *MNRAS*, 418, L79, doi: [10.1111/j.1745-3933.2011.01147.x](https://doi.org/10.1111/j.1745-3933.2011.01147.x)
- Tetarenko, B. E., Sivakoff, G. R., Heinke, C. O., & Gladstone, J. C. 2016, *ApJS*, 222, 15, doi: [10.3847/0067-0049/222/2/15](https://doi.org/10.3847/0067-0049/222/2/15)

- Timmes, F. X., Woosley, S. E., & Weaver, T. A. 1996, *ApJ*, 457, 834, doi: [10.1086/176778](https://doi.org/10.1086/176778)
- Tsuna, D., & Kawanaka, N. 2019, *MNRAS*, 488, 2099, doi: [10.1093/mnras/stz1809](https://doi.org/10.1093/mnras/stz1809)
- Tsuna, D., Kawanaka, N., & Totani, T. 2018, *MNRAS*, 477, 791, doi: [10.1093/mnras/sty699](https://doi.org/10.1093/mnras/sty699)
- van den Heuvel, E. P. J. 1992, Endpoints of stellar evolution: the incidence of stellar mass black holes in the Galaxy., In *ESA, Environment Observation and Climate Modelling Through International Space Projects. Space Sciences with Particular Emphasis on High-Energy Astrophysics* p 29-36 (SEE N93-23878 08-88)
- Vernetto, S., & Lipari, P. 2016, *PhRvD*, 94, 063009, doi: [10.1103/PhysRevD.94.063009](https://doi.org/10.1103/PhysRevD.94.063009)
- Vos, J., Cerutti, B., Moscibrodzka, M., & Parfrey, K. 2024, arXiv e-prints, arXiv:2410.19061, doi: [10.48550/arXiv.2410.19061](https://doi.org/10.48550/arXiv.2410.19061)
- Wong, G. N., Ryan, B. R., & Gammie, C. F. 2021, *ApJ*, 907, 73, doi: [10.3847/1538-4357/abd0f9](https://doi.org/10.3847/1538-4357/abd0f9)
- Yang, H., Hare, J., Kargaltsev, O., Volkov, I., & Chen, S. 2023, in *AAS/High Energy Astrophysics Division*, Vol. 20, AAS/High Energy Astrophysics Division, 116.84
- Yuan, F., & Narayan, R. 2014, *ARA&A*, 52, 529, doi: [10.1146/annurev-astro-082812-141003](https://doi.org/10.1146/annurev-astro-082812-141003)
- Zhang, H., Sironi, L., Giannios, D., & Petropoulou, M. 2023, *ApJL*, 956, L36, doi: [10.3847/2041-8213/acfe7c](https://doi.org/10.3847/2041-8213/acfe7c)
- Zhu, K. R., Chen, J. M., Zheng, Y. G., & Zhang, L. 2024, *MNRAS*, 527, 1794, doi: [10.1093/mnras/stad2813](https://doi.org/10.1093/mnras/stad2813)